Bulletin of the Seismological Society of America, Vol. 103, No. 3, pp. 1662–1678, June 2013, doi: 10.1785/0120120291

# Monitoring a Building Using Deconvolution Interferometry. I: Earthquake-Data Analysis

by Nori Nakata, Roel Snieder, Seiichiro Kuroda, Shunichiro Ito, Takao Aizawa, and Takashi Kunimi

**Abstract** For health monitoring of a building, we need to separate the response of the building to an earthquake from the imprint of soil-structure coupling and from wave propagation below the base of the building. Seismic interferometry based on deconvolution, where we deconvolve the wave fields recorded at different floors, is a technique to extract this building response and thus estimate velocity of the wave that propagates inside the building. Deconvolution interferometry also allows us to estimate the damping factor of the building. Compared with other interferometry techniques, such as cross-correlation and cross-coherence interferometry, deconvolution interferometry is the most suitable technique to monitor a building using earthquake records. For deconvolution interferometry, we deconvolve the wave fields recorded at all levels with the waves recorded at a target receiver inside the building. This receiver behaves as a virtual source, and we retrieve the response of a cut-off building, a short building that is cut off at the virtual source. Because the cut-off building is independent from the structure below the virtual source, the technique might be useful for estimating local structure and local damage. We apply deconvolution interferometry to 17 earthquakes recorded during two weeks at a building in Fukushima, Japan, and estimate time-lapse changes in velocity and normal-mode frequency. As shown in a previous study, the change in velocity correlates with the change in normal-mode frequency. We compute the velocities from both traveling waves and the fundamental mode using coda-wave interferometry. These velocities have a negative correlation with the maximum acceleration of the observed earthquake records.

## Introduction

The response of a building to an earthquake has been studied since the early 1900s (e.g., Biot, 1933; Sezawa and Kanai, 1935; Carder, 1936). We can estimate the frequencies of the fundamental and higher modes of buildings using ambient and forced vibration experiments (Trifunac, 1972; Ivanović *et al.*, 2000; Kohler *et al.*, 2005; Clinton *et al.*, 2006; Michel *et al.*, 2008). Because of the shaking caused by major earthquakes, the frequencies of normal modes decrease (Trifunac *et al.*, 2001a; Kohler *et al.*, 2005); the reduction is mostly temporary (a few minutes) and healing occurs with time, but some reduction is permanent. Clinton *et al.*, 2006 found more than 20% temporal reduction and 4% permanent reduction in the fundamental frequency of the motion of the Millikan Library located at the California Institute of Technology after the 1987 $M_L$ 5.9 Whittier Narrows earthquake. The reduction in the frequency logarithmically correlates with the maximum acceleration of observed records (Clinton *et al.*, 2006). Precipitation, strong wind, temperature, reinforcement, and heavy weight loaded in a building also change the frequencies of normal modes (Kohler *et al.*, 2005; Clinton *et al.*, 2006). Because these frequencies are related to both the building itself and the soil-structure coupling, we have to consider soil-structure interactions (Şafak, 1995) and nonlinearities in the response of the foundation soil (Trifunac *et al.*, 2001a,b). Normal-mode frequencies estimated from observed records are, therefore, not suitable for health monitoring of a building in isolation of its environment (Todorovska and Trifunac, 2008b).

Snieder and Şafak (2006) show that one can estimate an impulse response independent from the soil-structure coupling and the complicated wave propagation (e.g., attenuation and scattering) below the bottom receiver by using seismic interferometry based on deconvolution. Seismic interferometry is a technique to extract the Green's function, which accounts for the wave propagation between receivers (Lobkis and Weaver 2001; Derode *et al.*, 2003; Snieder, 2004; Paul *et al.*, 2005; Snieder, Wapenaar, *et al.*, 2006; Wapenaar and Fokkema, 2006). Seismic interferometry can be based on cross correlation, deconvolution, and cross coherence (Snieder *et al.*, 2009; Wapenaar *et al.*, 2010). Deconvolution interferometry is a

useful technique for monitoring structures, especially in one dimension (Nakata and Snieder, 2011, 2012a,b). Because deconvolution interferometry changes the boundary condition at the base of the building, we are able to extract the pure response of the building regardless of its coupling to the subsurface (Snieder and Şafak, 2006; Snieder, Sheiman, *et al.*, 2006).

Deconvolution interferometry has been applied to earthquake records observed in a building to retrieve the velocity of traveling waves and attenuation of the building (Oyunchimeg and Kawakami, 2003; Snieder and Şafak, 2006; Kohler *et al.*, 2007; Todorovska and Trifunac, 2008a,b; some studies call the method impulse response function or normalized input–output minimization). Todorovska and Trifunac (2008b) use 11 earthquakes occurring over a period of 24 years to monitor the fundamental frequency of a building after applying deconvolution interferometry. The fundamental frequencies they estimated from the interferometry are always higher than the frequencies obtained from the observed records because the frequencies computed from the observed records are affected by both the building itself and soil-building coupling, whereas the frequencies estimated using the interferometry are only related to the building itself. Oyunchimeg and Kawakami (2003) apply short-time moving-window seismic interferometry to an earthquake record to estimate the velocity reduction of a building during an earthquake. Prieto *et al.* (2010) apply deconvolution interferometry to ambient vibrations after normalizing amplitudes per frequency using the multitaper method (Thomson, 1982) to estimate the traveling-wave velocity and damping factor.

In this study, we apply deconvolution interferometry to 17 earthquakes observed at a building in Japan over a period of two weeks and monitor the changes in velocity of the building. This study is based on the work of Snieder and Şafak (2006); furthermore, we extend the deconvolution interferometry as proposed by Snieder and Şafak (2006) to deconvolution with the waveforms recorded at an arbitrary receiver, compare this with cross-correlation and cross-coherence interferometry, and use interferometry for monitoring a building in Japan. First, we introduce our data: geometry of receivers, locations of the building and epicenters of earthquakes used, observed waveforms, and shapes of the normal modes extracted from observed records. We also introduce the equations of interferometry based on deconvolution, cross correlation, and cross coherence. We further indicate the deconvolved waveforms obtained from one earthquake and estimate a velocity as well as a quality factor ($Q$). Next, we apply deconvolution interferometry to all observed earthquakes and monitor the change in velocity of the building using coda-wave interferometry (Snieder *et al.*, 2002). In a companion paper, we apply the interferometry to ambient vibrations.

## Building and Earthquakes

The building (rectangle in Fig. 1) in which we recorded vibrations is located in the Fukushima prefecture, Japan.

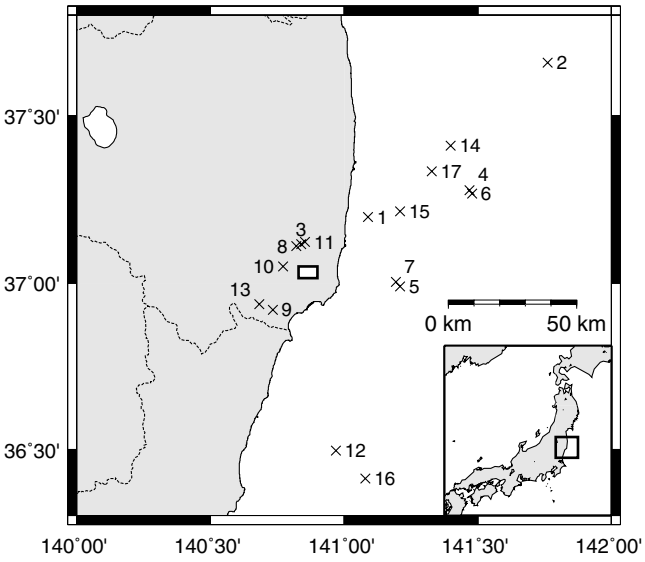


**Figure 1.** The building (rectangle, not to scale) and epicenters of earthquakes used (crosses). Numbers beside crosses correspond to the sequential numbers in Table 1. Inset indicates the location of the magnified area.

Continuous seismic vibrations were recorded by Suncoh Consultants Co., Ltd., for two weeks using 10 microelectromechanical-systems (MEMS) accelerometers, which were developed by Akebono Brake Industry Co., Ltd., and 17 earthquakes were observed during the two weeks (Table 1; Fig. 1). In this study, we focus on processing of the earthquake records, and we analyze ambient vibrations in the companion paper. The building includes eight stories, a basement, and a penthouse (Fig. 2). We installed receivers on the stairs, located 20 m from the east side and at the center between the north and south sides. The sampling interval of the records is 1 ms, and the receivers have three components. Here, we use two horizontal components, which are aligned with the east–west (EW) and north–south (NS) directions.

Figure 3a–d illustrates the observed waveforms and their power spectra of earthquake number 5, which gives the greatest acceleration to the building. Figure 3e,f shows the spectrogram of the motion at the fourth floor computed with the continuous-wavelet transform (Torrence and Compo, 1998). Higher frequencies quickly attenuate and the fundamental mode is dominant for later times in Figure 3e,f. The frequency of the fundamental mode in the EW component (1.17 Hz) is higher than the frequency in the NS component (0.97 Hz) because the EW side of the building is longer than the NS side. Both components have large amplitudes at around 0.5 Hz between 14 and 21 s. Because the 0.5 Hz component is localized in time (Fig. 3e,f), it corresponds to a surface wave that moves the entire building. Because the frequency of the surface wave is less than that of the fundamental mode of the building, however, it does not excite waves that propagate within the building.

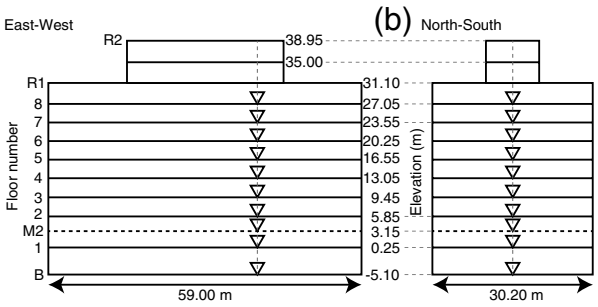


**Figure 2.** The (a) EW and (b) NS vertical cross sections of the building and the positions of receivers (triangles). Elevations denote the height of each floor from ground level. We put receivers on stairs 0.19 m below each floor except for the basement (on the floor) and the first floor (0.38 m below). Receiver M2 is located between the first and second floors. Horizontal-receiver components are aligned with the EW and NS directions.

Figure 4 illustrates the shapes of the normal-mode displacement computed from the real part of the Fourier spectra at different floors. We calculate displacement from acceleration using numerical integration (Schiff and Bogdanoff, 1967). Just as for the fundamental mode, the frequencies of overtones in the EW component are also higher than those in the NS component. Although the displacements of both components in mode 1 (the fundamental mode) are almost the same, the NS component displacement is larger than that of the EW component in modes 2 and 3. The amplitude of mode 1 is much larger than the amplitudes of other modes.

## Deconvolution with an Arbitrary Receiver

By deconvolving observed earthquake records, we obtain the impulse response of a building (Oyunchimeg and Kawakami, 2003; Snieder and Şafak, 2006; Kohler *et al.*, 2007; Todorovska and Trifunac, 2008a). When the height of the building is $H$, the recorded signal of an earthquake in the frequency domain at an arbitrary receiver at height $z$ is given by Snieder and Şafak (2006):

$$u(z) = \sum_{m=0}^{\infty} S(\omega)R^m(\omega)\{e^{ik(2mH+z)}e^{-\gamma|k|(2mH+z)} + e^{ik(2(m+1)H-z)}e^{-\gamma|k|(2(m+1)H-z)}\} = \frac{S(\omega)\{e^{ikz}e^{-\gamma|k|z} + e^{ik(2H-z)}e^{-\gamma|k|(2H-z)}\}}{1 - R(\omega)e^{2ikH}e^{-2\gamma|k|H}}, \quad (1)$$

where $S(\omega)$ is the incoming waveform to the base of the building, $R(\omega)$ is the reflection coefficient related to the coupling of the ground and the base of the building, $k$ is the wavenumber, $\gamma$ is the attenuation coefficient, and $i$ is the imaginary unit. We use the absolute value of wavenumbers in the damping terms because the waves attenuate regardless of whether the wavenumber is positive or negative. In equation (1), we assume that the wave propagates vertically in the building (one-dimensional propagation) with constant amplitude and wavenumber and without internal reflections. The constant wavenumber implies that we assume constant velocity $c$ because $k = \omega/c$. The incoming waveform $S(\omega)$ includes the source signature of the earthquake and the effect of propagation such as attenuation and scattering along the

Table 1
Origin Times, Magnitudes, and Hypocenter Locations of Recorded Earthquakes Estimated by the Japan Meteorological Agency (JMA)

| Number | Origin Time (yyyy/mm/dd hh:mm:ss.s) | $M_{JMA}$ | Latitude | Longitude | Depth (km) | Maximum Acceleration (m/s$^2$) |
|---|---|---|---|---|---|---|
| 1 | 2011/05/31 16:12:20.2 | 3.9 | 37.1983 | 141.0900 | 32 | 0.145 |
| 2 | 2011/06/01 01:41:19.6 | 4.2 | 37.6583 | 141.7617 | 44 | 0.088 |
| 3 | 2011/06/01 06:23:27.2 | 3.4 | 37.1167 | 140.8400 | 7 | 0.061 |
| 4 | 2011/06/03 21:44:38.7 | 4.2 | 37.2783 | 141.4683 | 36 | 0.040 |
| 5 | 2011/06/04 01:00:14.1 | 5.5 | 36.9900 | 141.2100 | 30 | 1.923 |
| 6 | 2011/06/04 09:03:33.7 | 4.3 | 37.2683 | 141.4783 | 36 | 0.147 |
| 7 | 2011/06/04 10:41:10.0 | 4.1 | 37.0033 | 141.1933 | 28 | 0.083 |
| 8 | 2011/06/05 17:32:38.9 | 3.5 | 37.1117 | 140.8217 | 7 | 0.281 |
| 9 | 2011/06/05 19:46:06.3 | 3.9 | 36.9200 | 140.7333 | 14 | 0.175 |
| 10 | 2011/06/05 20:16:37.0 | 4.4 | 37.0500 | 140.7717 | 11 | 0.843 |
| 11 | 2011/06/07 03:11:55.9 | 2.6 | 37.1233 | 140.8540 | 5 | 0.020 |
| 12 | 2011/06/09 19:38:32.9 | 5.7 | 36.4967 | 140.9700 | 13 | 0.358 |
| 13 | 2011/06/11 00:40:55.4 | 3.9 | 36.9367 | 140.6833 | 11 | 0.075 |
| 14 | 2011/06/11 01:41:19.6 | 3.9 | 37.4117 | 141.3983 | 46 | 0.087 |
| 15 | 2011/06/12 05:08:58.4 | 4.5 | 37.2150 | 141.2100 | 21 | 0.153 |
| 16 | 2011/06/12 17:09:45.4 | 4.6 | 36.4117 | 141.0800 | 47 | 0.270 |
| 17 | 2011/06/13 05:59:35.1 | 4.4 | 37.3350 | 141.3283 | 33 | 0.180 |

The earthquakes are numbered sequentially according to their origin times. Maximum acceleration is the observed maximum amplitude of the MEMS accelerometers at the first floor in the 120 s following the origin time of each earthquake.

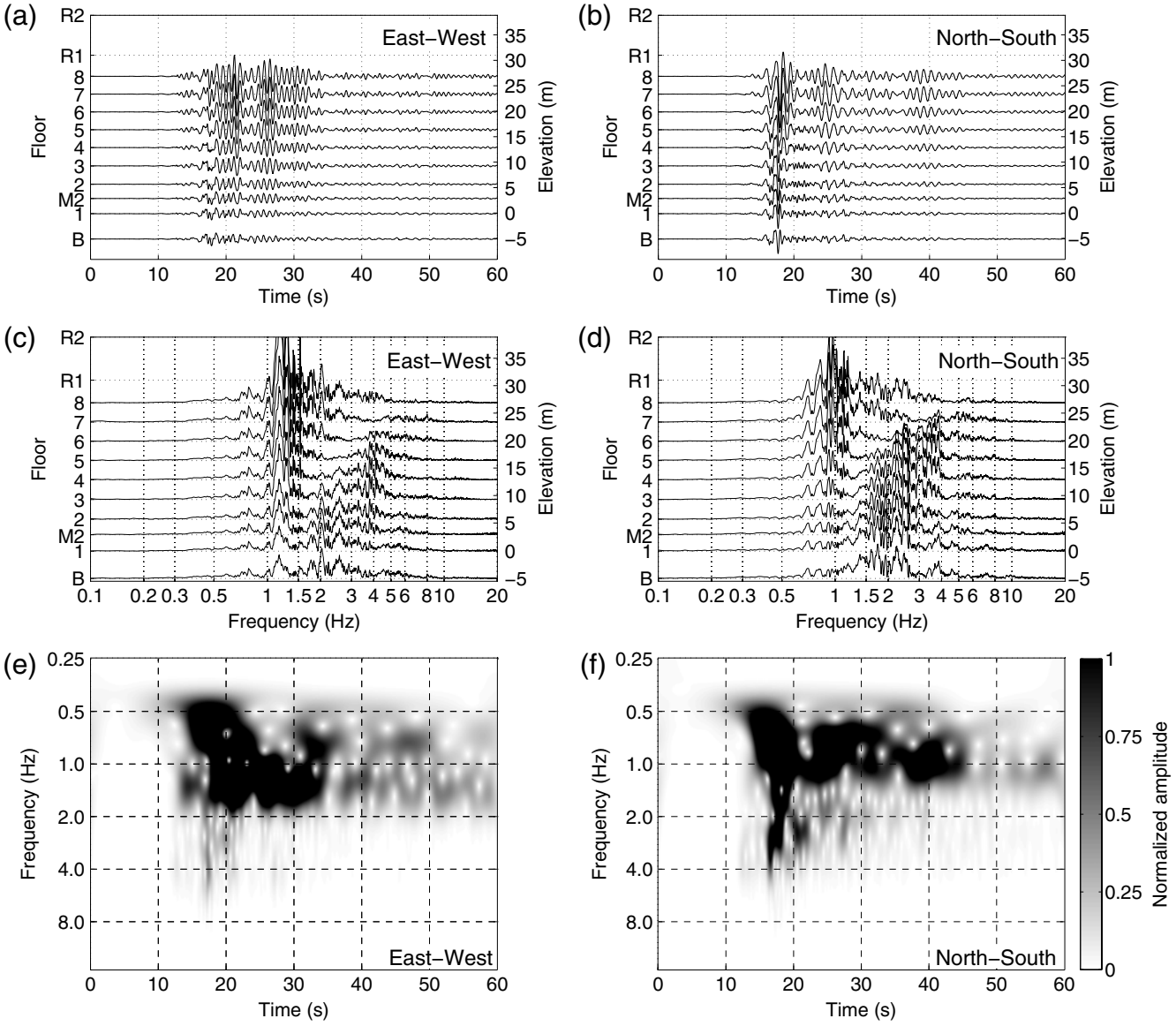


**Figure 3.** Unfiltered waveforms of earthquake number 5 recorded at the building in (a) the EW component and (b) the NS component, and (c, d) their power spectra. (e, f) Spectrogram computed with continuous-wavelet transformed waveforms recorded at the fourth floor. Time 0 s represents the origin time of the earthquake. We preserve relative amplitudes of the EW and NS components.

path from the hypocenter of the earthquake to the base of the building. The attenuation coefficient $\gamma$ is defined as

$$\gamma = \frac{1}{2Q}, \tag{2}$$

with $Q$ the quality factor (Aki and Richards, 2002).

For $m = 0$ in the first line in equation (1), the first term $S(\omega)e^{ikz}e^{-\gamma|k|z}$ indicates the incoming upgoing wave and the second term $S(\omega)e^{ik(2H-z)}e^{-\gamma|k|(2H-z)}$ the downgoing wave, which is reflected off the top of the building. The index $m$ represents the number of reverberations between the base and top of the building.

As we deconvolve a waveform recorded by a receiver at $z$ with a waveform observed by another receiver at $z_a$, from equation (1) we obtain

$$\begin{aligned} D(z, z_a, \omega) &= \frac{u(z)}{u(z_a)} \\ &= \frac{S(\omega)\{e^{ikz}e^{-\gamma|k|z} + e^{ik(2H-z)}e^{-\gamma|k|(2H-z)}\}}{S(\omega)\{e^{ikz_a}e^{-\gamma|k|z_a} + e^{ik(2H-z_a)}e^{-\gamma|k|(2H-z_a)}\}} \\ &= \sum_{n=0}^{\infty}(-1)^n\{e^{ik(2n(H-z_a)+z-z_a)}e^{-\gamma|k|(2n(H-z_a)+z-z_a)} \\ &\quad + e^{ik(2n(H-z_a)+2H-z-z_a)} \\ &\quad \times e^{-\gamma|k|(2n(H-z_a)+2H-z-z_a)}\}, \end{aligned} \tag{3}$$

where we use a Taylor expansion in the last equality. In equation (3), the receiver at $z_a$ behaves as a virtual source. Equation (3) may be unstable because of the spectral division. In practice we use a regularization parameter $\varepsilon$ (Yilmaz, 2001, Section 2.3):

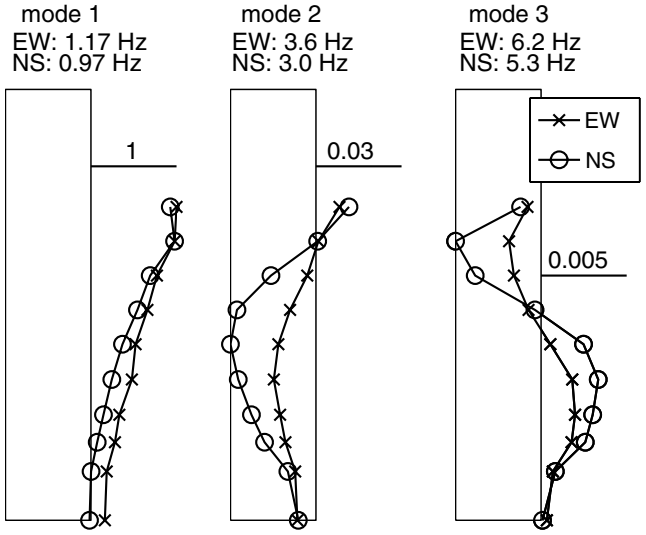


**Figure 4.** Displacement of the first three horizontal normal modes for earthquake number 5 estimated from the real part of the Fourier spectra at different floors. Each mark indicates the displacement of a receiver. The center frequency of each mode is shown at the top of each panel. Black horizontal lines and the numbers on the lines show the amplitude ratio among modes, and the box depicts the height of the building (R2 in Fig. 2). The zero displacement is at the right side of each box.

$$D(z, z_a, \omega) = \frac{u(z)}{u(z_a)} \approx \frac{u(z)u^*(z_a)}{|u(z_a)|^2 + \varepsilon\langle|u(z_a)|^2\rangle}, \qquad (4)$$

where * is a complex conjugate and $\langle|u(z_a)|^2\rangle$ is the average power spectrum of $u(z_a)$. In this study we use $\varepsilon = 1\%$.

Note that these deconvolved waves are independent of the incoming waveform $S(\omega)$ and the ground coupling $R(\omega)$. When we consider substitutions $S(\omega) \to 1$, $R(\omega) \to -1$, $H \to H - z_a$, and $z \to z - z_a$, equation (1) reduces to equation (3). These conditions indicate the physical properties of the deconvolved waveforms: impulse response ($S(\omega) \to 1$), perfect reflection at the virtual source ($R(\omega) \to -1$), and a small building ($H \to H - z_a$ and $z \to z - z_a$), as we discuss later.

When $z > z_a$, equation (3) describes a wave that is excited at $z_a$ and reverberates between $z_a$ and the top of the building. Using a normal-mode analysis (equation A4 in Appendix A), the fundamental mode of equation (3) in the time domain is given by

$$D(z, z_a, t) = \frac{4\pi c}{H - z_a} e^{-\gamma\omega_0 t} \sin(\omega_0 t) \cos\left(\omega_0 \frac{H - z}{c}\right), \qquad (5)$$

where $\omega_0 = \pi c/\{2(H - z_a)\}$. The period of the fundamental mode is, thus,

$$T_0 = \frac{4(H - z_a)}{c}, \qquad (6)$$

which corresponds to the period of the fundamental mode of the building that is cut off at $z_a$ (cut-off building; Fig. 5a). According to equation (3) the polarity change resulting from

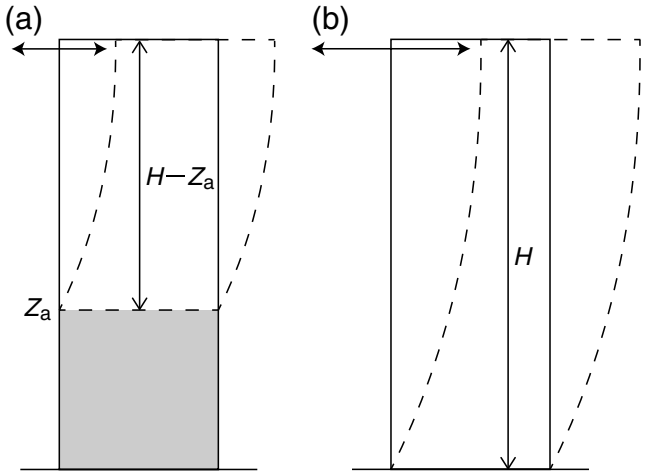


**Figure 5.** Schematic shapes of the fundamental mode retrieved by using seismic interferometry. (a) Fundamental mode retrieved by deconvolving wave fields with a motion recorded at $z_a$ (equation 3). (b) Fundamental mode retrieved by deconvolving wave fields with a motion recorded at the first floor (equation 9).

reflection at $z_a$ is given by $(-1)^n$, the reflection coefficient at the virtual source is $-1$. Therefore, the cut-off building is only sensitive to the properties of the building above $z_a$, and the reconstructed wave motion in the cut-off building has the potential to estimate local structure and local damage instead of structure and damage for the entire building.

When $z < z_a$ and $n = 0$ in equation (3) we obtain two waves: an acausal upgoing wave from $z$ to $z_a$ ($e^{ik(z-z_a)}e^{-\gamma|k|(z-z_a)}$) and a causal downgoing wave from $z_a$ to $z$ ($e^{ik(2H-z-z_a)}e^{-\gamma|k|(2H-z-z_a)}$). Waves for $n \geq 1$ in equation (3) account for the reverberations between $z_a$ and the top of the building. Because $D(z_a, z_a, \omega) = 1$, the deconvolved waveforms at $z_a$ is a delta function in the time domain ($D(z_a, z_a, t) = \delta(t)$); thus, $D(z_a, z_a, t) = 0$ for $t \neq 0$ (clamped boundary condition; Snieder, Sheiman, *et al.*, 2006; Snieder *et al.*, 2009). The upgoing and downgoing waves interfere destructively at $z_a$.

Although we assume, for simplicity, a constant velocity in equation (1), we can apply deconvolution interferometry to wave fields observed at a building with smoothly varying velocities. When the velocity $c$ varies with height, the local wavenumber does so as well, and using the WKBJ approximation for the phase, equation (1) generalizes to

$$u(z) = \frac{U}{1 - R(\omega)\exp(2i\int_0^H k(z)dz)\exp(-2\gamma\int_0^H |k(z)|dz)} \qquad (7)$$

with

$$U = S(\omega)\left[\exp\left(i\int_0^z k(z)dz\right)\exp\left(-\gamma\int_0^z |k(z)|dz\right) + \exp\left\{i\left(\int_0^H k(z)dz + \int_z^H k(z)dz\right)\right\} \times \exp\left\{-\gamma\left(\int_0^H |k(z)|dz + \int_z^H |k(z)|dz\right)\right\}\right],$$

and equation (3) generalizes in this case to

$$D(z,z_a,\omega)=\sum_{n=0}^{\infty}(-1)^n\left[\exp\left\{i\left(2n\int_{z_a}^{H}k(z)dz+\int_{z_a}^{z}k(z)dz\right)\right\}\right.$$
$$\times\exp\left\{-\gamma\left(2n\int_{z_a}^{H}|k(z)|dz+\int_{z_a}^{z}|k(z)|dz\right)\right\}$$
$$+\exp\left\{i\left((2n+1)\int_{z_a}^{H}k(z)dz+\int_{z}^{H}k(z)dz\right)\right\}$$
$$\times\exp\left\{-\gamma\left((2n+1)\int_{z_a}^{H}|k(z)|dz\right.\right.$$
$$\left.\left.\left.+\int_{z}^{H}|k(z)|dz\right)\right\}\right]. \quad (8)$$

As for equation (3), equation (8) represents the waves in a cut-off building at $z_a$, and the period of the fundamental mode of the cut-off building depends on the slowness averaged between $z_a$ and $H$. Note that when $z > z_a$, $D(z,z_a,\omega)$ in equation (8) is only related to $k(z)$ above $z_a$.

When $z_a$ is at the first floor ($z_a = 0$) or at the top of the building ($z_a = H$), equation (3) corresponds to equations (26) or (21) in Snieder and Şafak (2006), respectively, which we rewrite here as

$$D(z,0,\omega)=\sum_{n=0}^{\infty}(-1)^n\{e^{ik(2nH+z)}e^{-\gamma|k|(2nH+z)}$$
$$+e^{ik(2(n+1)H-z)}e^{-\gamma|k|(2(n+1)H-z)}\}, \quad (9)$$

$$D(z,H,\omega)=\frac{1}{2}\{e^{ik(H-z)}e^{-\gamma|k|(H-z)}+e^{-ik(H-z)}e^{\gamma|k|(H-z)}\}. \quad (10)$$

if the building were placed on a rigid subsurface (i.e., the reflection coefficient at the base is $-1$). When we put a receiver at the top floor (8 in Fig. 2) of a building instead of the rooftop ($R_1$ or $R_2$ in Fig. 2), we theoretically do not obtain the response in equation (10) because the traveling waves reflect at the top of the building rather than at the top floor. In this case, the deconvolved response follows equation (3). This difference may be insignificant when the wavelength of the traveling waves is much longer than the distance between the top floor and the top of the building.

## Cross-Correlation and Cross-Coherence Interferometry

In the previous section, we focused on seismic interferometry based on deconvolution. Let us consider seismic interferometry based on cross correlation (e.g., Schuster *et al.*, 2004) and cross coherence (e.g., Nakata *et al.*, 2011); these two methods are the techniques applied most widely and applied earliest (Aki, 1957), respectively.

### Cross Correlation

From equation 1, the cross correlation of $u(z)$ and $u(z_a)$ is

$$C(z,z_a,\omega)=u(z)u^*(z_a)$$
$$=|S(\omega)|^2\frac{\{e^{ikz}e^{-\gamma|k|z}+e^{ik(2H-z)}e^{-\gamma|k|(2H-z)}\}\{e^{-ikz_a}e^{-\gamma|k|z_a}+e^{-ik(2H-z_a)}e^{-\gamma|k|(2H-z_a)}\}}{1-R(\omega)e^{2ikH}e^{-2\gamma|k|H}-R^*(\omega)e^{-2ikH}e^{-2\gamma|k|H}+|R(\omega)|^2e^{-4\gamma|k|H}}. \quad (11)$$

In contrast to the deconvolution (equation 3), equation (11) depends on the incoming wave $S(\omega)$ and the ground coupling $R(\omega)$ and does not create a clamped boundary condition ($C(z_a,z_a,\omega)\neq 1$). Because of the presence of the reflection coefficient $R(\omega)$ and the power spectrum $|S(\omega)|^2$, it is much more complicated to estimate the properties (e.g., traveling-wave velocity and attenuation) of the building from cross correlation than from deconvolution.

When $z_a = 0$ and $z_a = H$, equation (11) reduces to

$$C(z,0,\omega)=|S(\omega)|^2\frac{e^{ikz}e^{-\gamma|k|z}+e^{-ikz}e^{-\gamma|k|(4H-z)}+e^{ik(2H-z)}e^{-\gamma|k|(2H-z)}+e^{-ik(2H-z)}e^{-\gamma|k|(2H+z)}}{1-R(\omega)e^{2ikH}e^{-2\gamma|k|H}-R^*(\omega)e^{-2ikH}e^{-2\gamma|k|H}+|R(\omega)|^2e^{-4\gamma|k|H}}, \quad (12)$$

$$C(z,H,\omega)=2|S(\omega)|^2\frac{e^{-2\gamma|k|H}\{e^{ik(H-z)}e^{-\gamma|k|(H-z)}+e^{-ik(H-z)}e^{\gamma|k|(H-z)}\}}{1-R(\omega)e^{2ikH}e^{-2\gamma|k|H}-R^*(\omega)e^{-2ikH}e^{-2\gamma|k|H}+|R(\omega)|^2e^{-4\gamma|k|H}}, \quad (13)$$

Figure 5b illustrates a schematic shape of the fundamental mode as given in equation (9). The period of the mode in equation (9) is related to the structure of the entire building as

respectively. If $R(\omega) = 0$ (no reflection at the base), equation (13) is, apart from the prefactor $2|S(\omega)|^2e^{-2\gamma|k|H}$, the same as equation (10).

Cross Coherence

Cross coherence is defined as frequency-normalized cross correlation:

$$CH(z, z_a, \omega) = \frac{u(z)u^*(z_a)}{|u(z)||u(z_a)|} \approx \frac{u(z)u^*(z_a)}{|u(z)||u(z_a)| + \varepsilon' \langle |u(z)||u(z_a)| \rangle}. \quad (14)$$

Similar to equation (4), we use a regularization parameter $\varepsilon'$ in the last equality in practice. In this study, we use $\varepsilon' = 0.1\%$. For mathematical interpretation, using Taylor expansions of $\sqrt{1+X}$ and $1/\sqrt{1+X}$ for $X < 1$, the cross coherence between $u(z)$ and $u(z_a)$ is given by

$$\begin{aligned} CH(z, z_a, \omega) &= \frac{u(z)u^*(z_a)}{|u(z)||u(z_a)|} = \frac{u(z)u^*(z_a)}{\sqrt{u(z)u^*(z)}\sqrt{u(z_a)u^*(z_a)}} = \frac{\sqrt{u(z)}\sqrt{u^*(z_a)}}{\sqrt{u^*(z)}\sqrt{u(z_a)}} \\ &= \sqrt{\frac{\{e^{ikz}e^{-\gamma|k|z} + e^{ik(2H-z)}e^{-\gamma|k\ (2H-z)}\}\{e^{-ikz_a}e^{-\gamma|k|z_a} + e^{-ik(2H-z_a)}e^{-\gamma|k|(2H-z_a)}\}}{\{e^{-ikz}e^{-\gamma|k|z} + e^{-ik(2H-z)}e^{-\gamma|k|(2H-z)}\}\{e^{ikz_a}e^{-\gamma|k|z_a} + e^{ik(2H-z_a)}e^{-\gamma|k|(2H-z_a)}\}}} \\ &= e^{ik(z-z_a)} \times \left[1 + \frac{1}{2}\sum_{n=1}^{\infty}\left\{\frac{e^{2ink(H-z)}e^{-2n\gamma|k|(H-z)}}{n!}A_{n-1}\right\}\right] \\ &\quad \times \left[1 + \frac{1}{2}\sum_{n=1}^{\infty}\left\{\frac{e^{-2ink(H-z_a)}e^{-2n\gamma|k|(H-z_a)}}{n!}A_{n-1}\right\}\right] \\ &\quad \times \left[1 + \sum_{n=1}^{\infty}\left\{\frac{e^{-2ink(H-z)}e^{-2n\gamma|k|(H-z)}}{n!}A_{n}\right\}\right] \\ &\quad \times \left[1 + \sum_{n=1}^{\infty}\left\{\frac{e^{2ink(H-z_a)}e^{-2n\gamma|k|(H-z_a)}}{n!}A_{n}\right\}\right], \end{aligned} \quad (15)$$

where $A_0 = 1$ and $A_n = (2n-1)!!/(-2)^n$. As for deconvolution interferometry, equation (15) does not depend on $S(\omega)$ and $R(\omega)$. For a complex number $z = re^{i\phi}$, the square root is defined as $\sqrt{z} = \sqrt{r}e^{i\phi/2}$. Furthermore, the waveforms of cross-coherence interferometry satisfies a clamped boundary condition at $z = z_a$ ($CH(z_a, z_a, \omega) = 1$, thus, $CH(z_a, z_a, t) = \delta(t)$, and $CH(z_a, z_a, t) = 0$ for $t \neq 0$).

For $z_a = 0$ and $z_a = H$, equation (15) simplifies to

$$\begin{aligned} CH(z,0,\omega) &= e^{ikz} \times \left[1 + \frac{1}{2}\sum_{n=1}^{\infty}\left\{\frac{e^{2ink(H-z)}e^{-2n\gamma|k|(H-z)}}{n!}A_{n-1}\right\}\right] \\ &\quad \times \left[1 + \frac{1}{2}\sum_{n=1}^{\infty}\left\{\frac{e^{-2inkH}e^{-2n\gamma|k|H}}{n!}A_{n-1}\right\}\right] \\ &\quad \times \left[1 + \sum_{n=1}^{\infty}\left\{\frac{e^{-2ink(H-z)}e^{-2n\gamma|k|(H-z)}}{n!}A_{n}\right\}\right] \\ &\quad \times \left[1 + \sum_{n=1}^{\infty}\left\{\frac{e^{2inkH}e^{-2n\gamma|k|H}}{n!}A_{n}\right\}\right], \end{aligned} \quad (16)$$

$$\begin{aligned} CH(z, H, \omega) &= e^{ik(z-H)} \times \left[1 + \frac{1}{2}\sum_{n=1}^{\infty}\left\{\frac{e^{2ink(H-z)}e^{-2n\gamma|k|(H-z)}}{n!}A_{n-1}\right\}\right] \\ &\quad \times \left[1 + \sum_{n=1}^{\infty}\left\{\frac{e^{-2ink(H-z)}e^{-2n\gamma|k|(H-z)}}{n!}A_{n}\right\}\right], \end{aligned} \quad (17)$$

respectively. Note that because of the complexity of cross-coherence interferometry, equations (15)–(17) contain pseudoevents that propagate at slower velocities than the true velocity of the building. For example, equation (16) can be expanded into

$$\begin{aligned} CH(z,0,\omega) = e^{ikz}&\left\{1 - \frac{1}{4}e^{-4\gamma|k|(H-z)} - \frac{1}{4}e^{-4\gamma|k|H}\right\} \\ &+ \frac{1}{4}e^{-ikz}e^{-2\gamma|k|(2H-z)} + \frac{1}{4}e^{3ikz}e^{-2\gamma|k|(2H-z)} \\ &- \frac{1}{2}e^{-ik(2H-3z)}e^{-2\gamma|k|(H-z)} - \frac{1}{2}e^{ik(2H+z)}e^{-2\gamma|k|H} \\ &+ \frac{1}{2}e^{ik(2H-z)}e^{-2\gamma|k|(H-z)} + \frac{1}{2}e^{-ik(2H-z)}e^{-2\gamma|k|H} \\ &+ \frac{3}{8}e^{-ik(4H-5z)}e^{-4\gamma|k|(H-z)} - \frac{1}{8}e^{-ik(4H-z)}e^{-4\gamma|k|H} \\ &- \frac{1}{4}e^{ik(4H-z)}e^{-2\gamma|k|(2H-z)} + \frac{3}{8}e^{-ik(4H-z)}e^{-4\gamma|k|H} \\ &- \frac{1}{8}e^{ik(4H-3z)}e^{-4\gamma|k|(H-z)} - \frac{1}{4}e^{-ik(4H-3z)} \\ &\times e^{-2\gamma|k|(2H-z)} + O(e^{-6\gamma|k|(H-z)}). \end{aligned} \quad (18)$$

The terms $e^{3ikz}e^{-2\gamma|k|(2H-z)}/4$ and $-e^{-ik(2H-3z)}e^{-2\gamma|k|(H-z)}/2$ indicate waves that propagate at one-third of the true velocity, and the term $3e^{-ik(4H-5z)}e^{-4\gamma|k|(H-z)}/8$ at

Table 2
Amplitudes of Traveling Waves Obtained from Observed Records and Computed by Seismic Interferometry Based on Deconvolution, Cross Correlation, and Cross Coherence for $z_a = 0$ (Equations 1, 9, 12, and 16)

| Phase | Observed Record | Deconvolution | Cross Correlation | Cross Coherence |
|---|---|---|---|---|
| $e^{ikz}$ | $S(\omega)e^{-\gamma\|k\|z}$ | $e^{-\gamma\|k\|z}$ | $C_1$ | $1-\frac{1}{4}e^{-4\gamma\|k\|(H-z)}-\frac{1}{4}e^{-4\gamma\|k\|H}$ |
| $e^{ik(2H-z)}$ | $S(\omega)e^{-\gamma\|k\|(2H-z)}$ | $e^{-\gamma\|k\|(2H-z)}$ | $C_2$ | $\frac{1}{2}e^{-2\gamma\|k\|(H-z)}$ |
| $e^{ik(2H+z)}$ | $S(\omega)R(\omega)e^{-\gamma\|k\|(2H+z)}$ | $-e^{-\gamma\|k\|(2H+z)}$ | $C_3$ | $-\frac{1}{2}e^{-2\gamma\|k\|H}$ |
| $e^{ik(4H-z)}$ | $S(\omega)R(\omega)e^{-\gamma\|k\|(4H-z)}$ | $-e^{-\gamma\|k\|(4H-z)}$ | $C_4$ | $-\frac{1}{4}e^{-2\gamma\|k\|(2H-z)}$ |

$C_1 = |S(\omega)|^2 e^{-\gamma|k|z}\{1+R(\omega)e^{-4\gamma|k|H}\}\{\sum_{n=0}^{\infty}|R(\omega)|^{2n}e^{-4n\gamma|k|H}\}$
$C_2 = |S(\omega)|^2 e^{-\gamma|k|(2H-z)}\{1+R(\omega)e^{-4\gamma|k|H}\}\{\sum_{n=0}^{\infty}|R(\omega)|^{2n}e^{-4n\gamma|k|H}\}$
$C_3 = |S(\omega)|^2 R(\omega)e^{-\gamma|k|(2H+z)}\{1+R(\omega)e^{-4\gamma|k|H}\}\{\sum_{n=0}^{\infty}|R(\omega)|^{2n}e^{-4n\gamma|k|H}\}$
$C_4 = |S(\omega)|^2 R(\omega)e^{-\gamma|k|(4H-z)}\{1+R(\omega)e^{-4\gamma|k|H}\}\{\sum_{n=0}^{\infty}|R(\omega)|^{2n}e^{-4n\gamma|k|H}\}$
We compute the amplitudes of cross-correlation interferometry in Appendix B. For cross-coherence interferometry, we ignore wave fields that attenuate faster than $e^{-6\gamma|k|(H-z)}$.

one-fifth. These unphysical waves complicate the estimation of the velocity of traveling waves by applying cross-coherence interferometry to earthquake data.

### Comparison of Deconvolution, Cross Correlation, and Cross Coherence

Each type of interferometry has different properties (e.g., amplitude or complexity). It follows from equations (4), (11), and (14) that in the frequency domain the phases obtained by interferometry based on deconvolution, cross correlation, and cross coherence are the same. The spectral amplitude is different, though, and this leads to different waveforms in the time domain. We list in Table 2 the amplitudes of the first four causal waves propagating at the true velocity of the building for observed record, deconvolution, cross correlation, and cross coherence (equations 1, 9, 12, and 16, respectively). For cross-correlation interferometry, we calculate the amplitudes of the traveling waves in Appendix B using Taylor expansions. Although the amplitudes of cross correlation are complicated due to the reflection coefficient $R(\omega)$ and the power spectrum $|S(\omega)|^2$, the ratios of amplitudes for each pair of traveling waves are the same as those for observed records. The amplitudes of the waveforms obtained by cross coherence are independent of incoming waveform $S(\omega)$ and reflection coefficient $R(\omega)$, but the ratio of amplitudes varies between each pair of traveling waves. Therefore, estimating attenuation of the building using cross-coherence interferometry is problematic. Because the amplitudes of the deconvolved waveforms are independent of $S(\omega)$ and $R(\omega)$ and depend exponentially on the traveled distance, deconvolution interferometry can be used to estimate attenuation of the building.

We numerically compute synthetic waveforms excited at 0 m by an impulsive source ($S(\omega) = 1$) based on equation (1) shown in Figure 6a. In the computation, we use the following parameters: $H = 100$ m, $R(\omega) = 0.5$, $Q = 3000$, and $c = 200$ m/s. In applying seismic interferometry, we compute deconvolution $(\{u(z)u^*(0)\}/\{|u(0)|^2 + \varepsilon\langle|u(0)|^2\rangle\})$; Fig. 6b), cross correlation $(u(z)u^*(0)$; Fig. 6c), and cross coherence $(\{u(z)u^*(0)\}/\{|u(z)||u(0)| + \varepsilon'\langle|u(z)||u(0)|\rangle\}$; Fig. 6d), where $\varepsilon = 1\%$ and $\varepsilon' = 0.1\%$, using the synthetic waveforms shown in Figure 6a. In Figure 6b–d, the virtual source is at $z = 0$ m. Deconvolved waveforms (Fig. 6b) arrive at the same time as the waves in the synthetic records, but the polarization is reversed when the wave is reflected at $z = 0$ m due to the clamped boundary condition. In cross-correlation interferometry (Fig. 6c), the causal waves arrive at the same time as the waves in the synthetic records (Fig. 6a), and the acausal waves are kinematically identical to the time-reversed causal waves. Although for simplicity we use $S(\omega) = 1$ in Figure 6, the incoming wave complicates the cross-correlated waveforms when we use real earthquake data, and picking the arrival times of the traveling waves may be difficult in that case. Cross-coherence interferometry creates traveling waves that propagate at slower velocities than true velocity $c = 200$ m/s. In Figure 6d, the gray line highlights the wave $-e^{-ik(2H-3z)}e^{-2\gamma|k|(H-z)}/2$, which travels with one-third of the true wave speed (66.7 m/s). To estimate the velocity of the traveling waves, therefore, deconvolution interferometry is useful.

We highlight the amplitudes of the waves in Figure 6 with the circles. A comparison of Figure 6a and 6b shows that the ratios of the amplitudes of the synthetic records and deconvolved waves within the first two circles are the same, but the ratios in the second and third circles are different. The reflection coefficient at 0 m of the synthetic records is $R(\omega)$, whereas the reflection coefficient of waves obtained by deconvolution interferometry is $-1$; see the numbers next to the arrows in Figure 6a and 6b. The difference between the reflection coefficients implies that deconvolved waveforms are independent of the ground coupling, and the decay of amplitudes of the waves is only related to the attenuation of the building. The ratios of the amplitudes of the waves highlighted by the circles in cross-correlation interferometry are the same as those in the synthetic records; see the numbers next to the arrows in Figure 6a and 6c. Thus, both the building and the soil-structure coupling influence the amplitudes of cross-correlated waveforms. In cross-coherence

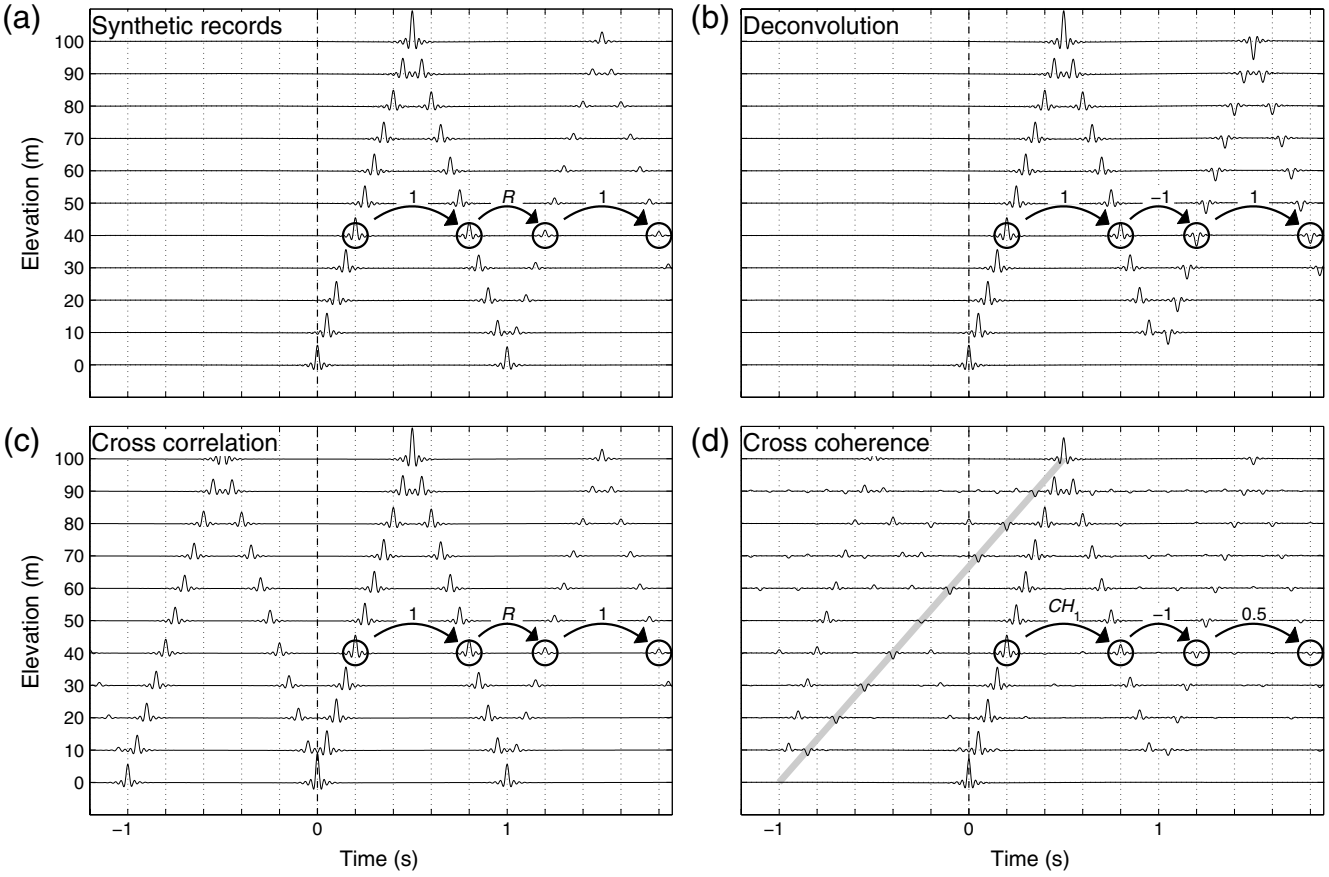


**Figure 6.** (a) Synthetic waveforms based on equation (1). We numerically calculate waveforms with an impulse response ($S(\omega) = 1$) at $t = 0$ s at 0 m, $R(\omega) = 0.5$, $Q = 3000$, $H = 100$ m, and $c = 200$ m/s. Interferometric waveforms by computing deconvolution (panel b: equation 9), cross correlation (panel c: equation 12), and cross coherence (panel d: equation 16) using waveforms shown in panel (a). The virtual source for interferometry is at the 0 m receiver. We apply a bandpass filter 0.5–1–30–40 Hz after computing each waveform. The circles in each panel highlight four waves, which are discussed in the main text. The numbers near each arrow indicate the ratio of the amplitude difference between two waves highlighted by the circles apart from the attenuation expected from the traveling distance at the correct velocity. To estimate the ratio of amplitude in panel (d), we ignore wave fields that attenuate faster than $e^{-6\gamma|k|(H-z)}$, and $CH_1 = 2/(4 - e^{-4\gamma|k|(H-z)} - e^{-4\gamma|k|H})$ where $z = 40$ m. Amplitudes in each panel are normalized by the amplitude of the first highlighted wave (at $t = 0.2$ s). The gray line in panel (d) shows the wave that propagates at 66.67 m/s.

interferometry (Fig. 6d), the ratios of the amplitudes of the waves within the circles are different from either synthetic records or deconvolution interferometry. When we consider the amplitudes of each interferometry, deconvolution interferometry is useful for estimating the attenuation of the building.

Based on equations (11)–(18), Table 2, and Figure 6, we conclude that deconvolution interferometry is suitable for application to earthquake records to estimate the velocity and attenuation of the building. Cross-correlated waveforms depend on the incoming wave $S(\omega)$ and the ground coupling $R(\omega)$. Cross-coherence interferometry creates pseudoevents, and the decay of amplitudes of waveforms reconstructed by cross coherence is not exponentially depending on the traveled distances. Therefore, these types of interferometry are not appropriate to estimate velocity and attenuation.

Snieder, Sheiman, *et al.* (2006) show that the wave fields obtained from deconvolution interferometry satisfy the same wave equation as the wave field of the real building for an external source. Using this idea, we explain why cross-coherence interferometry creates unphysical events. Following Snieder, Sheiman, *et al.* (2006), we denote the linear differential operator that defines the wave propagation by $L(z)$ (e.g., for the one-dimensional wave equation $L(z) = d^2/dz^2 + \omega^2/c^2(z)$). The operator acts on the space variable $z$. For an internal source at $z_0$, the wave field $u(z)$ (equation 1) satisfies $L(z)u(z) = F(z_0)$ where $F$ is the excitation at $z_0$. For an external source, on the other hand, $u(z)$ satisfies $L(z)u(z) = 0$; this homogeneous equation applies to earthquake data. Applying the operator $L(z)$ to equations (3), (11), and (14), respectively, gives

$$L(z)D(z, z_a, \omega) = L(z)\frac{u(z)}{u(z_a)} = \frac{1}{u(z_a)}L(z)u(z) = 0, \quad (19)$$

$$L(z)C(z, z_a, \omega) = L(z)u(z)u^*(z_a) = \{L(z)u(z)\}u^*(z_a) = 0, \quad (20)$$

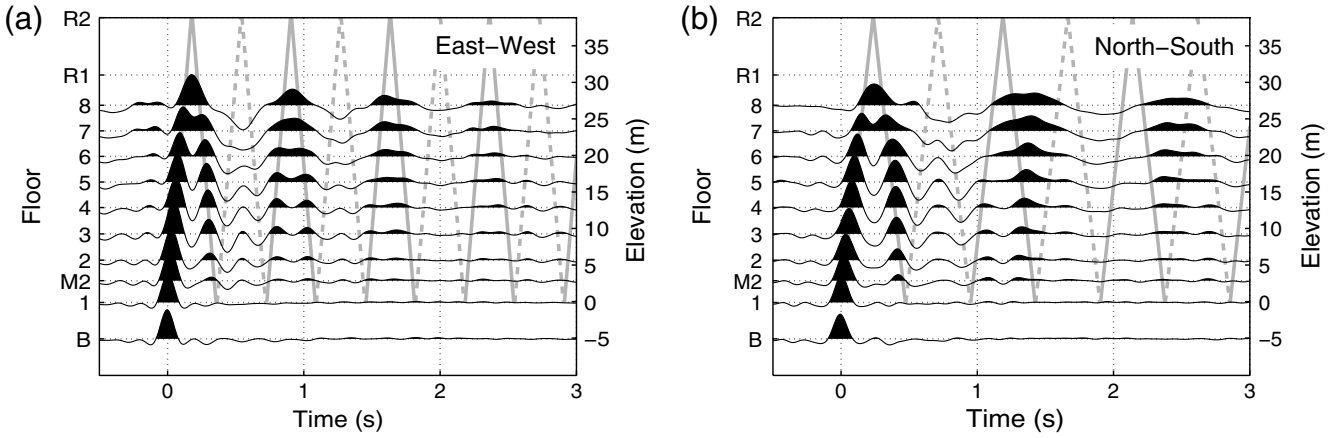


**Figure 7.** Deconvolved waveforms, in which the virtual source is at the first floor, of earthquake number 5 after applying a bandpass filter 0.4–0.5–45–50 Hz in the (a) EW and (b) NS components. Arrival time of traveling waves with the velocity that is estimated from the least-squares fitting of the first upgoing and downgoing waves, gray lines. We repeat the gray lines after the second traveling waves based on equation (9). Waves in the positive polarization, solid gray lines; waves in the negative polarization, dashed gray lines.

$$L(z)CH(z,z_a,\omega) = L(z)\frac{u(z)u^*(z_a)}{|u(z)||u(z_a)|} = \frac{u^*(z_a)}{|u(z_a)|}L(z)\left(\frac{u(z)}{|u(z)|}\right) \neq 0, \qquad (21)$$

where $L(z)$ acts on the $z$ coordinate only. Cross-coherence interferometry (equation 21) does not produce a wave field that satisfies the wave equation of the real building, but deconvolution and cross-correlation interferometry do satisfy the wave equation. Equation 21 shows that cross-coherence interferometry creates unphysical internal sources that complicate wave fields obtained from cross coherence.

## Deconvolved Waveforms Generated from an Earthquake

As an illustration of the data analysis, we first show the application of deconvolution interferometry to the records of earthquake number 5. We first estimate whether the reflection point of the traveling wave is at R1 or R2 because the building has a penthouse (Fig. 2). Figure 7 shows waveforms deconvolved by the motion recorded at the first floor (equation 9) for the EW and NS components. We apply a 0.4–0.5–45–50 Hz sine-squared bandpass filter to the deconvolved waveforms. Because the physical property at the basement is different from the other floors, we do not deconvolve with the motion in the basement in this study. During the first several-hundred milliseconds in Figure 7, the waveforms depict a traveling wave excited at the first floor at $t = 0$ s. The wave is reflected off the top of the building and propagates down, and then reflects again at the first floor with the opposite polarization because the reflection coefficient of the deconvolved waves at the first floor is equal to $-1$ (according to equation 9). While reverberating between the first floor and the top of the building, higher frequencies attenuate and the fundamental mode is dominant for later times.

To estimate the velocity of the traveling wave and the location of the reflection point, we compute the travel-time curve using a least-squares fitting of the picked travel times on the first upgoing and downgoing waves at each floor (the first two solid gray lines in Fig. 7). For picking the travel times, we seek the maximum amplitude time in each traveling wave. We repeatedly draw the reverberating travel-wave paths based on equation (9) using the velocity estimated from the first upgoing and downgoing waves (in Fig. 7). To avoid large uncertainties we use the picked travel times between floors one through five in the EW component and between floors one through six in the NS component because at these floors the positive amplitudes of the upgoing and downgoing waves do not overlap. Both travel-time curves in the EW and NS components indicate that the waves reflect off the top of the penthouse (R2), and the velocity is $214 \pm 9$ m/s in the EW direction and $158 \pm 7$ m/s in the NS direction, respectively, where the uncertainties are one standard deviation of measurements. Because the NS side is shorter, the velocity in the NS component is slower. The deconvolved waveforms in the NS component show large deviation from expected arrival times shown in the gray lines in Figure 7b, which indicates that the frequency dispersion in the NS component is larger than in the EW component. In the following, we focus on the EW component analysis.

In Appendix C, we apply cross-correlation and cross-coherence interferometry to records in the EW component. Because of the power spectrum of the incoming wave, we cannot obtain traveling waves using cross-correlation interferometry (Fig. C1c in Appendix C). We can estimate the velocity of traveling waves from the waveforms created by cross-coherence interferometry, but cannot estimate attenuation because the fundamental mode is not reconstructed (Fig. C1d in Appendix C).

Next, we deconvolve the wave fields with the motion recorded by the receiver at the fourth floor (Fig. 8), where

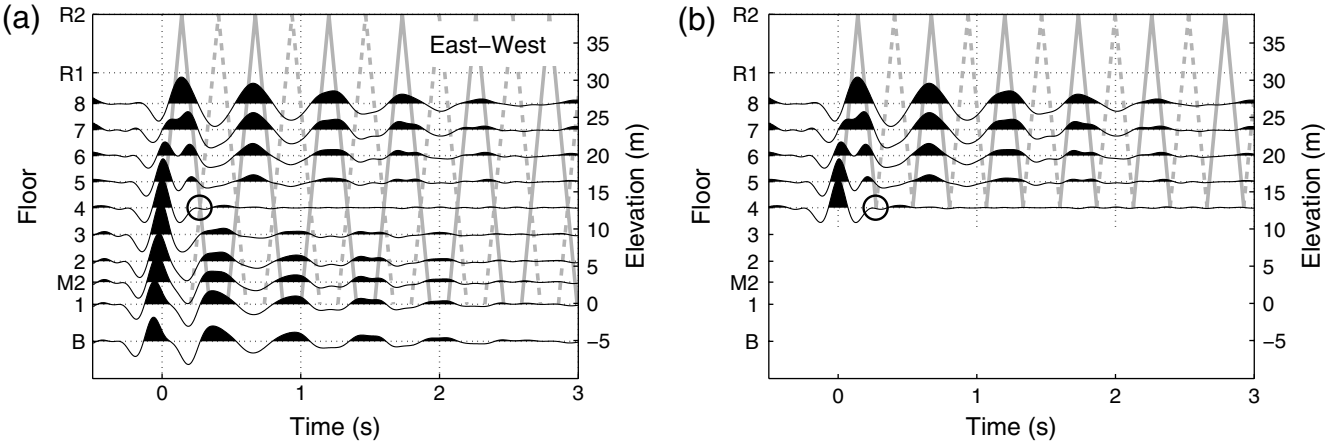


**Figure 8.** (a) Deconvolved waveforms, in which the virtual source is at the fourth floor, of earthquake number 5 after applying a bandpass filter 0.4–0.5–45–50 Hz in the EW component. Travel paths expected from the velocity 195 m/s and equation (3), gray lines. Waves in the positive polarization, solid gray lines; waves in the negative polarization, dashed gray lines. The point where the positive and negative polarization waves cancel, circle. (b) The same waveforms shown in panel (a) but with the deconvolved waveforms lower than the fourth floor omitted. When we focus on the cut-off building above the fourth floor, the reflection coefficient at the circle is −1.

the fourth-floor receiver behaves as a virtual source and satisfies a clamped boundary condition; then we apply the same bandpass filter as used in Figure 7. We can interpret waveforms in Figure 8 in two ways, which are explained using Figure 8a,b. We obtain upgoing and downgoing waves, which interfere at the fourth floor. At the circle in Figure 8a, the upgoing wave from the bottom and downgoing wave from the top cancel, and the deconvolved waveform at the fourth floor vanishes for nonzero time, which is due to the fact that the waveform at the virtual source is a band-limited delta function.

The fourth floor also behaves as the reflection point with reflection coefficient −1 (equation 3), which means we can separate the building into two parts: above and below the virtual source. Figure 8b shows the building above the virtual source. At the circle in Figure 8b, the downgoing wave with positive polarization from the top is perfectly reflected as the negative-polarization upgoing wave. Because we obtain an upgoing wave from the virtual source and reverberations between the fourth floor and the top of the building, this example of interferometry creates the response of a cut-off building that is independent from the structure below the fourth floor (see equation 3 and Fig. 8b). Similar to Figure 7, the fundamental mode for the cut-off building (equation 3 and Fig. 5a) is dominant for later times in Figure 8b. Note the similarity between Figures 7a and 8b; both figures show traveling waves and fundamental mode. The period of the normal mode in Figure 8b is shorter than in Figure 7a as is expected from equation (6). Interestingly, because the cut-off building is independent from the structure below the fourth floor, this fictitious building is useful for detecting local structure and local damage of the building.

Applying a least-squares fit of the travel times of the first upgoing wave at the first to fourth floors ($n = 0$ and $0 \le z \le z_a$ in equation 3), we obtain the velocity of traveling waves to be 195 ± 25 m/s. To avoid large uncertainties, we use the travel times at the first to fourth floors to estimate the velocity. At these floors, the upgoing waves are well separated from the downgoing waves. For the cut-off building, by estimating the velocity from the deconvolved waveforms at the floors only below or above the virtual source, we can obtain the velocity that is only related to the structure below or above the virtual source because the virtual source satisfies the clamped boundary conditions. The structure between the first and fourth floors (below the virtual source) contributes to the estimation of this velocity. This is the main reason why the mean velocities estimated from Figures 7 and 8 differ, but this discrepancy is not statistically significant.

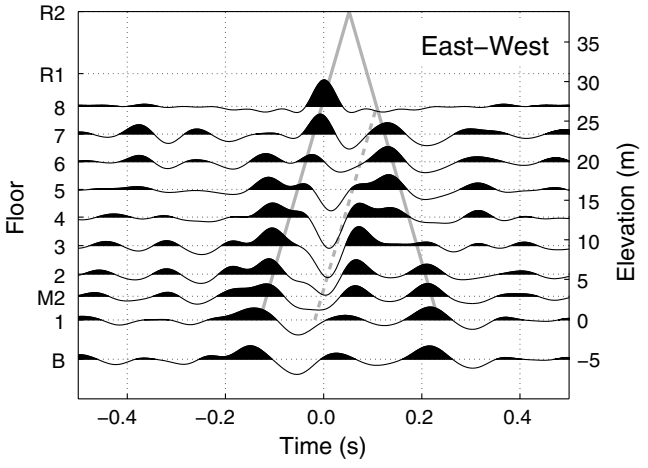


**Figure 9.** Deconvolved waveforms, in which the virtual source is at the eighth floor, of earthquake number 5 after applying a bandpass filter 0.4–0.5–12–16 Hz in the EW component. Travel time of the waves propagating at 210 m/s, gray lines. The positions of the lines are estimated from equation (3). Positive polarization, thick lines; negative polarization, dashed line.

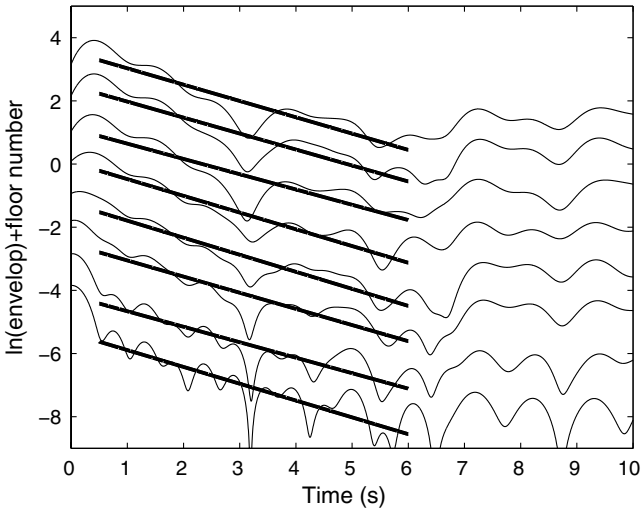


**Figure 10.** Natural logarithm of the envelopes, thin line; linear fitting using the least-squares method, thick line. We show envelopes at only the middle-second to eighth floors because the first floor is a virtual source and the basement floor has a different physical condition.

We apply deconvolution interferometry to the motion recorded by the receiver at the eighth floor, which is the highest receiver in the building (Fig. 9). Snieder and Şafak (2006) found that this procedure gives only one pair of upgoing and downgoing waves; because the eighth-floor receiver is ∼12 m below the top of the building (R2), however, the deconvolved waveforms in Figure 9 satisfy equation (3) instead of equation (10). In Figure 9, we apply a 0.4–0.5–12–16 Hz sine-squared bandpass filter to deconvolved waveforms. Because the quality of the data is not enough to accurately pick travel times, we cannot estimate the wave velocity from Figure 9. The gray lines in Figure 9 indicate the arrival time of the traveling waves at 210 m/s as inferred from Figure 7a.

From the resonant waves in Figures 7 and 8, we can estimate $Q$ following the method proposed by Snieder and Şafak (2006). Figure 10 shows the logarithmic envelopes of the deconvolved waveforms in Figure 7a at each floor except the basement and the first floor (thin lines), and their least-squares linear fits (thick lines). Because we use the waveforms deconvolved with the first floor, the estimated $Q$ is for the entire building. We assume $Q$ is constant in the entire building because the wavelength in the frequency range used is much longer than the height of the building (the resonant frequency is 1.17 Hz). In Figure 10, the average slope of the fitting lines indicates that $Q^{-1} = 0.098$ based on the fundamental-mode frequency 1.17 Hz.

## Monitoring a Building Using 17 Earthquakes

Using the 17 earthquakes recorded in the two weeks (Table 1 and Fig. 2), we monitor the change in the shear-wave velocity of the building. Figure 11 illustrates the waveforms that are deconvolved by the wave recorded at the first floor of each earthquake (Fig. 11a) and the power spectra of

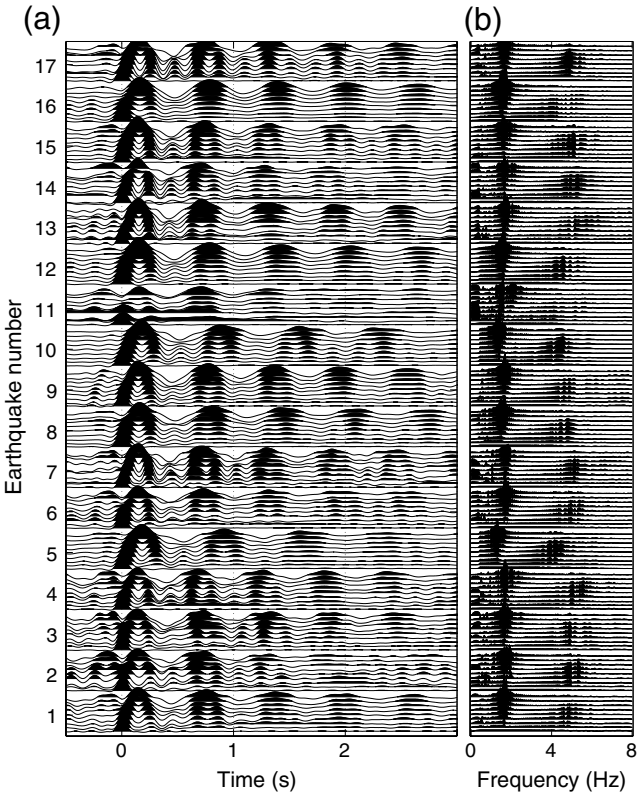


**Figure 11.** (a) The waveforms of each earthquake in the EW component after deconvolution with the waves recorded on the first floor in the time domain, and (b) the power spectra of the waveforms. We apply a bandpass filter 0.4–0.5–45–50 Hz. We show the traces from the first floor to the eighth floor in each earthquake.

the deconvolved waveforms (Fig. 11b). The virtual source is at the first floor (similar to Fig. 7a). The frequency component around 1.5 Hz shows the fundamental mode and around 5 Hz the first overtone. From the bottom to top traces for each earthquake, the traces are aligned from the first to eighth floors, and the waves propagating between the bottom and the top are visible. Comparing the fundamental-mode waves for later times among earthquakes, we can roughly estimate changes in velocity from a visual inspection, e.g., the velocities in earthquakes 5, 8, 10, and 12 are slower. The earthquakes, which show slower velocity, indicate lower normal-mode frequencies as shown by Todorovska and Trifunac (2008b). The ratio of the reductions in velocity and frequency are almost the same.

The amplitude of each resonant wave provides an estimate of attenuation. For example, the attenuation is strong for earthquake number 5 because the amplitude of the fundamental mode fades away at around 2.5 s. For some earthquakes, although the fundamental mode is dominant at later times, deconvolved waveforms still show upgoing and downgoing waves (e.g., at 2.5 s of earthquake number 15), which implies either that the attenuation at higher frequency is relatively weak at the time these earthquakes occurred, or that the overtones are strongly excited. We estimate the velocity of traveling waves using the method that is the same as for

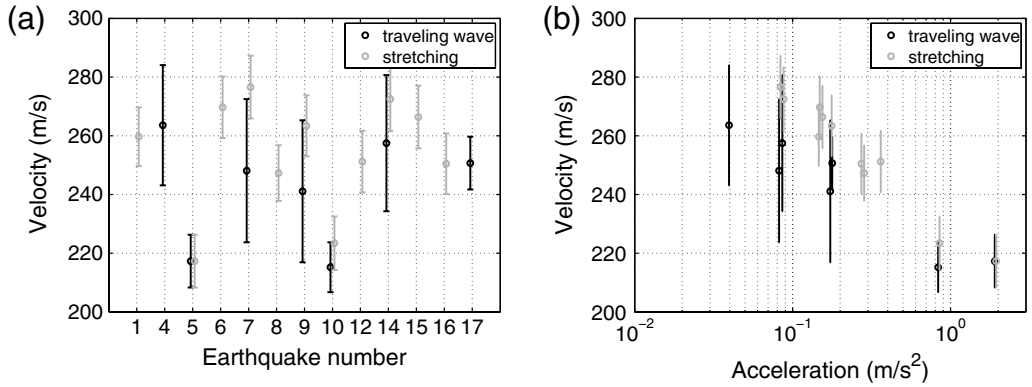


**Figure 12.** (a) Velocities estimated from traveling waves (black) and by coda-wave interferometry using the stretching method (gray) of each earthquake. The error bars of the velocities estimated from traveling waves (black) are one standard deviation of individual arrival times, and the bars in the stretching method are calculated by $\sqrt{\sigma_5^2 + \sigma_{\delta v}^2}$. We illustrate only velocities that have $< 10\%$ velocity uncertainty (for traveling waves) or are estimated from more than three traces that have a correlation coefficient $> 0.9$ (for the stretching method). (b) Cross plot of estimated velocities with maximum acceleration observed at the first floor.

Figure 7a (the black symbols in Fig. 12). The black marks in Figure 12b illustrate a negative correlation between the velocities and the maximum acceleration of observed records.

To estimate velocities, we also apply coda-wave interferometry as developed by Snieder *et al.* (2002) to deconvolved waveforms. Coda-wave interferometry allows us to estimate a relative velocity change from two waveforms by computing cross correlation. Coda-wave interferometry has been applied to multiplets (e.g., Poupinet *et al.*, 1984; Snieder and Vrijlandt, 2005) and to waveforms obtained by seismic interferometry (e.g., Sens-Schönfelder and Wegler, 2006). By using coda-wave interferometry, we estimate velocities from the deconvolved waves between 1 and 3 s in Figure 11. The waves in the time interval are mostly the fundamental mode. We choose earthquake number 5 as a reference and estimate the relative velocity for each earthquake from the reference earthquake. In coda-wave interferometry, we stretch and interpolate one waveform and compute a correlation coefficient (CC) with a reference waveform ($u_{\mathrm{ref}}$) in the time domain (Fig. 13; Lobkis and Weaver, 2003; Hadziioannou *et al.*, 2009; Weaver *et al.*, 2011):

$$CC(\alpha) = \frac{\int_{t_1}^{t_2} u(t(1-\alpha))u_{\mathrm{ref}}(t)dt}{\sqrt{\int_{t_1}^{t_2} u^2(t(1-\alpha))dt \int_{t_1}^{t_2} u_{\mathrm{ref}}^2(t)dt}}, \tag{22}$$

where $t_1$ and $t_2$ denote the time window, and in this study we use 1–3 s. At the maximum of $CC(\alpha)$,

$$\alpha = \frac{v - v_{\mathrm{ref}}}{v_{\mathrm{ref}}}, \tag{23}$$

where $v$ and $v_{\mathrm{ref}}$ are the velocities at each earthquake and the reference earthquake, respectively. For computing CC, we apply the same bandpass filter as for Figure 11, and the waves are mostly the fundamental mode.

Note that even though we use the waves between 1 and 3 s for applying coda-wave interferometry, the origin time for stretching is at time 0 s. The gray symbols in Figure 12 are the velocities estimated by coda-wave interferometry using

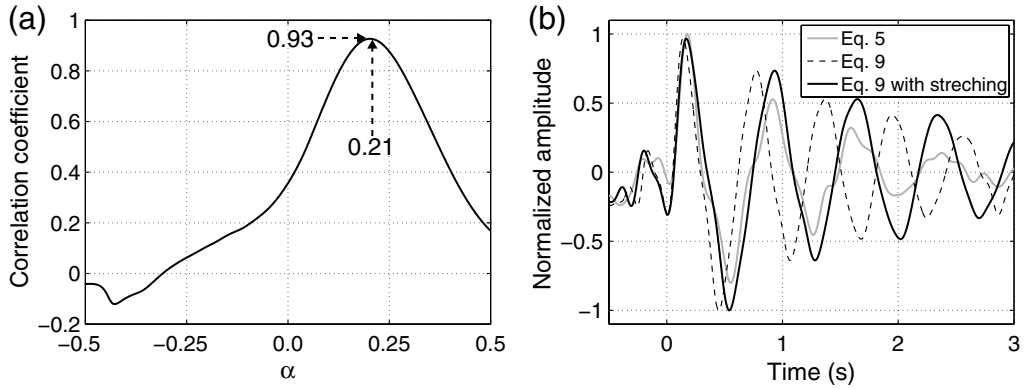


**Figure 13.** (a) Correlation coefficient (CC) as a function of $\alpha$ (equation 22) between deconvolved waveforms computed from earthquakes number 5 and number 9 at the eighth floor. Dashed arrows point to the maximum CC value and its value of $\alpha$. For computing CC, we use only the waveforms from 1.0 to 3.0 s. (b) Deconvolved waveforms at the eighth floor of earthquakes number 5, number 9, and number 9 with stretching for $\alpha = 0.21$ (see panel a).

the stretching method. Because we use earthquake number 5 as a reference ($u_{\mathrm{ref}}$), the estimated velocities of each earthquake using the stretching method (the gray symbols in Fig. 12) are the relative velocities with respect to the velocity of earthquake number 5. Therefore, the velocities estimated from traveling waves and by the stretching method in earthquake number 5 are, by definition, the same. The standard deviation of the velocity change (the gray bars in Fig. 12) for each earthquake is estimated by $\sqrt{\sigma_5^2 + \sigma_{\delta v}^2}$, where $\sigma_5$ is the standard deviation of the velocity measurements estimated from traveling waves at different floors in earthquake number 5, and $\sigma_{\delta v}$ is the standard deviation of the relative velocity measurements between each earthquake and earthquake number 5 estimated by the stretching method at different floors. The gray symbols in Figure 12b indicate that the velocities obtained by the stretching method also have a negative correlation with the acceleration, but the slope is steeper than that for the traveling waves. Because the waves in 1–3 s are mostly fundamental mode and the main difference between the traveling waves and the fundamental mode is the frequency (the traveling waves contain higher frequencies than the fundamental mode), the difference in slopes indicates dispersion. The steeper slope of the gray symbols in Figure 12b indicates that the imprint of acceleration is stronger for lower frequencies than for higher frequencies.

## Conclusions

We obtain impulse responses of the building and their changes in velocity by applying deconvolution interferometry to 17 earthquake records. We estimate the reflection point of the traveling wave, which is at the top of the penthouse, from the deconvolved waveforms. Because the shape of the ground plan of the building is rectangular, the velocities of the traveling wave in two orthogonal horizontal components are different. According to the properties of deconvolution, the responses are independent from the soil-structure coupling and the effect of wave propagation below the bottom receiver. Because the cut-off building is independent of the structure below the virtual source, one might be able to use the cut-off building to investigate local structure and local damage. Cross-correlation interferometry cannot separate the building response from the soil-building coupling and the wave propagation below the virtual source. Cross-coherence interferometry produces unphysical wave fields propagating at slower velocity than the true wave speed of the real building, and the attenuation of the waveforms obtained from cross coherence do not correspond to the travel distance of the waves. Thus, in contrast to deconvolution interferometry, these types of interferometry are not appropriate for applying to earthquake records for estimating velocities and attenuation of buildings. We estimate velocities from both traveling waves and the fundamental mode of deconvolved waveforms. The velocities estimated from each earthquake and maximum acceleration have a negative correlation.

## Data and Resources

Seismograms used in this study were operated and maintenanced by Suncoh Consultants Co., Ltd. Earthquake catalogs are listed at http://www.jma.go.jp (last accessed August 2012). Figure 1 is produced by using the Generic Mapping Tools (GMT; http://gmt.soest.hawaii.edu, last accessed August 2012).

## Acknowledgments

We are grateful to the sponsors of the Center for Wave Phenomena at the Colorado School of Mines. We thank JMA for providing the earthquake catalog. We are grateful to Diane Witters for her help in preparing this manuscript.

## References

Aki, K. (1957). Space and time spectra of stationary stochastic waves, with special reference to microtremors, *Bull. Earthq. Res. Inst.* **35,** 415–456.

Aki, K., and P. G. Richards (2002). *Quantitative Seismology*, Second Ed., University Science Books, 700 pp.

Biot, M. (1933). Theory of elastic systems vibrating under transient impulse with an application to earthquake-proof buildings, *Proc. Natl. Acad. Sci. Unit. States Am.* **19,** no. 2, 262–268.

Carder, D. S. (1936). Observed vibrations of buildings, *Bull. Seismol. Soc. Am.* **26,** no. 3, 245–277.

Clinton, J. F., S. C. Bradford, T. H. Heaton, and J. Favela (2006). The observed wander of the natural frequencies in a structure, *Bull. Seismol. Soc. Am.* **96,** no. 1, 237–257.

Derode, A., E. Larose, M. Campillo, and M. Fink (2003). How to estimate the Green's function of a heterogeneous medium between two passive sensors? Application to acoustic waves, *Appl. Phys. Lett.* **83,** no. 15, 3054–3056.

Hadziioannou, C., E. Larose, O. Coutant, P. Roux, and M. Campillo (2009). Satability of monitoring weak changes in multiply scattering media with ambient noise correlation: Laboratory experiments, *J. Acoust. Soc. Am.* **125,** no. 6, 3688–3695, doi: 10.1121/1.3125345.

Ivanović, S. S., M. D. Trifunac, and M. I. Todorovska (2000). Ambient vibration tests of structures—A review, *ISET J. Earthq. Tech.* **37,** no. 4, 165–197.

Kohler, M. D., P. M. Davis, and E. Şafak (2005). Earthquake and ambient vibration monitoring of the steel-frame UCLA Factor building, *Earthq. Spectra* **21,** no. 3, 715–736.

Kohler, M. D., T. H. Heaton, and S. C. Bradford (2007). Propagating waves in the steel, moment-frame factor building recorded during earthquakes, *Bull. Seismol. Soc. Am.* **97,** no. 4, 1334–1345.

Lobkis, O. I., and R. L. Weaver (2001). On the emergence of the Green's function in the correlations of a diffuse field, *J. Acoust. Soc. Am.* **110,** no. 6, 3011–3017.

Lobkis, O. I., and R. L. Weaver (2003). Coda-wave interferometry in finite solids: Recovery of P-to-S conversion rates in an elastodynamic billiard, *Phys. Rev. Lett.* **90,** no. 25, 254–302.

Michel, C., P. Guéguen, and P.-Y. Bard (2008). Dynamic parameters of structures extracted from ambient vibration measurements: An aid for the seismic vulnerability assessment of existing buildings in moderate seismic hazard regions, *Soil Dynam. Earthq. Eng.* **28,** 593–604.

Nakata, N., and R. Snieder (2011). Near-surface weakening in Japan after the 2011 Tohoku-Oki earthquake, *Geophys. Res. Lett.* **38,** L17302, doi: 10.1029/2011GL048800.

Nakata, N., and R. Snieder (2012a). Estimating near-surface shear-wave velocities in Japan by applying seismic interferometry to KiK-net data, *J. Geophys. Res.* **117,** B01308, doi: 10.1029/2011JB008595.

Nakata, N., and R. Snieder (2012b). Time-lapse change in anisotropy in Japan's near surface after the 2011 Tohoku-Oki earthquake, *Geophys. Res. Lett.* **39,** L11313, doi: 10.1029/2012GL051979.

Nakata, N., R. Snieder, T. Tsuji, K. Larner, and T. Matsuoka (2011). Shear-wave imaging from traffic noise using seismic interferometry by cross-coherence, *Geophysics* **76,** no. 6, SA97–SA106, doi: 10.1190/GEO2010-0188.1.

Oyunchimeg, M., and H. Kawakami (2003). A new method for propagation analysis of earthquake waves in damaged buildings: evolutionary normalized input-output minimization (NIOM), *J. Asian Archit. Build.* **2,** no. 1, 9–16.

Paul, A., M. Campillo, L. Margerin, and E. Larose (2005). Empirical synthesis of time-asymmetrical Green functions from the correlation of coda waves, *J. Geophys. Res.* **110,** B08302, doi: 10.1029/2004JB003521.

Poupinet, G., W. L. Ellsworth, and J. Frechet (1984). Monitoring velocity variations in the crust using earthquake doublets: An application to the Calaveras fault, California, *J. Geophys. Res.* **89,** no. B7, 5719–5731.

Prieto, G. A., J. F. Lawrence, A. I. Chung, and M. D. Kohler (2010). Impulse response of civil structures from ambient noise analysis, *Bull. Seismol. Soc. Am.* **100,** no. 5A, 2322–2328.

Şafak, E. (1995). Detection and identification of soil-structure interraction in buildings from vibration recordings, *J. Struct. Eng.* **121,** 899–906.

Schiff, A., and J. L. Bogdanoff (1967). Analysis of current methods of interpreting strong-motion accelerograms, *Bull. Seismol. Soc. Am.* **57,** no. 5, 857–874.

Schuster, G. T., J. Yu, J. Sheng, and J. Rickett (2004). Interferometric/daylight seismic imaging, *Geophys. J. Int.* **157,** 838–852.

Sens-Schönfelder, C., and U. Wegler (2006). Passive image interferometry and seasonal variations of seismic velocities at Merapi Volcano, Indonesia, *Geophys. Res. Lett.* **33,** L21302, doi: 10.1029/2006GL027797.

Sezawa, K., and K. Kanai (1935). Energy dissipation in seismic vibrations of actual buildings, *Bull. Earthq. Res. Inst.* **13,** 925–941.

Snieder, R. (2004). Extracting the Green's function from the correlation of coda waves: A derivation based on stationary phase, *Phys. Rev. E* **69,** 046610.

Snieder, R., and E. Şafak (2006). Extracting the building response using seismic interferometry: Theory and application to the Millikan library in Pasadena, California, *Bull. Seismol. Soc. Am.* **96,** no. 2, 586–598.

Snieder, R., and M. Vrijlandt (2005). Constraining the source separation with coda wave interferometry: Theory and application to earthquake doublets in the Hayward fault, California, *J. Geophys. Res.* **110,** B04301, doi: 10.1029/2004JB003317.

Snieder, R., A. Grêt, H. Douma, and J. Scales (2002). Coda wave interferometry for estimating nonlinear behavior in seismic velocity, *Science* **295,** 2253–2255.

Snieder, R., M. Miyazawa, E. Slob, I. Vasconcelos, and K. Wapenaar (2009). A comparison of strategies for seismic interferometry, *Surv. Geophys.* **30,** no. 10, 503–523.

Snieder, R., J. Sheiman, and R. Calvert (2006). Equivalence of the virtual-source method and wave-field deconvolution in seismic interferometry, *Phys. Rev. E* **73,** 066620.

Snieder, R., K. Wapenaar, and K. Larner (2006). Spurious multiples in seismic interferometry of primaries, *Geophysics* **71,** no. 4, SI111–SI124.

Thomson, D. J. (1982). Spectrum estimation and harmonic analysis, *Proc. IEEE* **70,** no. 9, 1055–1096.

Todorovska, M. I., and M. D. Trifunac (2008a). Earthquake damage detection in the Imperial Country Services Building III: Analysis of wave travel times via impulse response functions, *Soil Dynam. Earthq. Eng.* **28,** 387–404.

Todorovska, M. I., and M. D. Trifunac (2008b). Impulse response analysis of the Van Nuys 7-story hotel during 11 earthquakes and earthquake damage detection, *Struct. Contr. Health Monit.* **15,** 90–116.

Torrence, C., and G. P. Compo (1998). A practical guide to wavelet analysis, *Bull. Am. Meteorol. Soc.* **79,** no. 1, 61–78.

Trifunac, M. D. (1972). Comparisons between ambient and forced vibration experiments, *Earthq. Eng. Struc. Dynam.* **1,** 133–150.

Trifunac, M. D., S. S. Ivanović, and M. I. Todorovska (2001a). Apparent periods of a building. I: Fourier analysis, *J. Struct. Eng.* **127,** no. 5, 517–526.

Trifunac, M. D., S. S. Ivanović, and M. I. Todorovska (2001b). Apparent periods of a building. II: Time-frequency analysis, *J. Struct. Eng.* **127,** no. 5, 527–537.

Wapenaar, K., and J. Fokkema (2006). Green's function representations for seismic interferometry, *Geophysics* **71,** no. 4, SI33–SI46.

Wapenaar, K., D. Draganov, R. Snieder, X. Campman, and A. Verdel (2010). Tutorial on seismic interferometry: Part 1—Basic principles and applications, *Geophysics* **75,** no. 5, 75A195–75A209.

Weaver, R. L., C. Hadziioannou, E. Larose, and M. Campillo (2011). On the precision of noise correlation interferometry, *Geophys. J. Int.* **185,** 1384–1392.

Yilmaz, O. (2001). *Seismic Data Analysis, Investigations in Geophysics*, Vol. 10, Second Ed., Society of Exploration Geophysicists, Tulsa, Oklahoma, doi: 10.1190/1.9781560801580.

## Appendix A

### Normal-Mode Analysis of Deconvolution Interferometry

In equation (3), we analyze the deconvolution interferometry based on superposition of traveling waves using a Taylor expansion. Here, we analyze equation (3) based on summation of normal-mode waves while using contour integration as following the procedure proposed by Snieder and Şafak (2006). Applying the inverse Fourier transform to $D(z, z_a, \omega)$ and using the relationship $k = \omega/c$, the deconvolved response in the time domain is given by

$$D(z, z_a, t) = \int_{-\infty}^{\infty} \frac{e^{-i\omega(t-\frac{z}{c})}e^{-\gamma|\omega|\frac{z}{c}} + e^{-i\omega(t-\frac{2H-z}{c})}e^{-\gamma|\omega|\frac{2H-z}{c}}}{e^{i\omega\frac{z_a}{c}}e^{-\gamma|\omega|\frac{z_a}{c}} + e^{i\omega\frac{2H-z_a}{c}}e^{-\gamma|\omega|\frac{2H-z_a}{c}}} d\omega. \tag{A1}$$

For $t > (2H - z)/c$, the locations of poles ($\omega_\dagger$) of the integrand in equation (A1) are

$$\omega_\dagger = \omega_l(\pm 1 - i\gamma), \qquad (l = 0, 1, 2, \ldots), \tag{A2}$$

where the normal-mode frequencies are given by

$$\omega_l = \frac{(l + \frac{1}{2})\pi c}{H - z_a}. \tag{A3}$$

Using the residue theorem, equation (A1) can be written as the summation of normal-mode wave fields:

$$D(z, z_a, t) = \frac{4\pi c}{H - z_a} \sum_{l=0}^{\infty} (-1)^l e^{-\gamma\omega_l t} \sin(\omega_l t) \cos\left(\omega_l \frac{H - z}{c}\right). \tag{A4}$$

## Appendix B

### Amplitude of Cross-Correlation Interferometry

In this appendix, we compute the amplitude of the cross-correlated waveforms in equation (12). Using Taylor expansions, we rewrite equation (12) as

$$C(z,0,\omega) = |S(\omega)|^2\{e^{ikz}e^{-\gamma|k|z} + e^{-ikz}e^{-\gamma|k|(4H-z)} + e^{ik(2H-z)}e^{-\gamma|k|(2H-z)} + e^{-ik(2H-z)}e^{-\gamma|k|(2H+z)}\} \times \left\{\sum_{n=0}^{\infty}(R(\omega))^n e^{2inkH}e^{-2n\gamma|k|H}\right\} \times \left\{\sum_{m=0}^{\infty}(R^*(\omega))^m e^{-2imkH}e^{-2m\gamma|k|H}\right\}. \quad \text{(B1)}$$

Here, we focus only on the waves with phases $e^{ikz}$, $e^{ik(2H-z)}$, $e^{ik(2H+z)}$, and $e^{ik(4H-z)}$ and define their amplitudes as $C_1$, $C_2$, $C_3$, and $C_4$, respectively. From equation (B1), $C_1$ is obtained by

$$C_1 e^{ikz} = |S(\omega)|^2\Bigg[e^{ikz}e^{-\gamma|k|z}\sum_{n=0}^{\infty}\{(R(\omega))^n e^{2inkH} \times e^{-2n\gamma|k|H}(R^*(\omega))^n e^{-2inkH}e^{-2n\gamma|k|H}\} + e^{-ik(2H-z)}e^{-\gamma|k|(2H+z)}\sum_{n=0}^{\infty}\{(R(\omega))^{n+1}e^{2i(n+1)kH} \times e^{-2(n+1)\gamma|k|H}(R^*(\omega))^n e^{-2inkH}e^{-2n\gamma|k|H}\}\Bigg]$$

$$C_1 = |S(\omega)|^2 e^{-\gamma|k|z}\{1 + R(\omega)e^{-4\gamma|k|H}\} \times \left\{\sum_{n=0}^{\infty}|R(\omega)|^{2n}e^{-4n\gamma|k|H}\right\}. \quad \text{(B2)}$$

Similar to expression B2, we obtain $C_2$, $C_3$, and $C_4$ as

$$C_2 = |S(\omega)|^2 e^{-\gamma|k|(2H-z)}\{1 + R(\omega)e^{-4\gamma|k|H}\} \times \left\{\sum_{n=0}^{\infty}|R(\omega)|^{2n}e^{-4n\gamma|k|H}\right\}, \quad \text{(B3)}$$

$$C_3 = |S(\omega)|^2 R(\omega)e^{-\gamma|k|(2H+z)}\{1 + R(\omega)e^{-4\gamma|k|H}\} \times \left\{\sum_{n=0}^{\infty}|R(\omega)|^{2n}e^{-4n\gamma|k|H}\right\}, \quad \text{(B4)}$$

$$C_4 = |S(\omega)|^2 R(\omega)e^{-\gamma|k|(4H-z)}\{1 + R(\omega)e^{-4\gamma|k|H}\} \times \left\{\sum_{n=0}^{\infty}|R(\omega)|^{2n}e^{-4n\gamma|k|H}\right\}. \quad \text{(B5)}$$

## Appendix C

### Applying Cross-Correlation and Cross-Coherence Interferometry to Real Data

In Figure C1, we apply cross-correlation and cross-coherence interferometry to real data to draw figures similar to Figure 7a. When we use the same bandpass filter as for Figure 7, cross-correlation interferometry enhances the fundamental-mode frequency, and only the fundamental

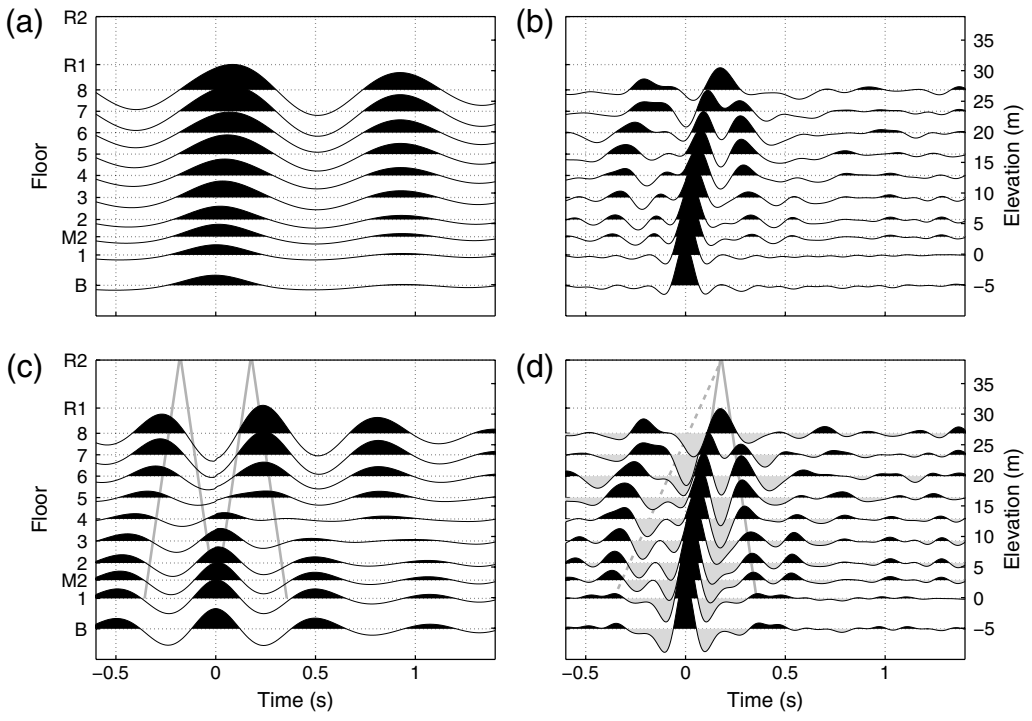


**Figure C1.** Waveforms obtained by applying (a, c) cross-correlation and (b, d) cross-coherence interferometry, in which the virtual source is at the first floor, to the records of earthquake number 5 in the EW component. These waveforms are applied bandpass filters (a, b) 0.4–0.5–45–50 Hz, (c) 1.3–1.6–45–50 Hz, and (d) 1.4–2–45–50 Hz. Note that the bandpass filter for panels (a) and (b) is the same filter as that used for Figure 7. The amplitude scales in each panel are different. The solid gray lines in panel (c) and (d) are the positive-polarity traveling waves with the velocity estimated from Figure 7a based on equations (12) and (16). The dashed gray line in panel (d) indicates the wave that propagates at one-third of the velocity of Figure 7a.

mode is visible (Fig. C1a). This is caused by the power spectrum of the incoming wave (equation 12). When we cut the fundamental-mode frequency, the first-higher mode is dominant in the cross-correlated waveforms (Fig. C1c). Therefore, we cannot estimate the velocity of traveling waves.

Figure C1b illustrates upgoing and downgoing waves from $t = 0$ s, and the waves propagate at the same velocity as the traveling waves reconstructed by deconvolution interferometry (Fig. 7a). These propagating waves, however, may be affected by the wave that propagates at slower velocities. The fundamental mode is not clear in Figure C1b because of the spectral ratio used in cross-coherence interferometry. As a result, the amplitude in later times is much smaller than the amplitude of deconvolution interferometry (Table 2). Because of the frequency we used, the wave propagating with slower velocity is not clear (the dashed gray line in Fig. C1d). The negative amplitudes around the dashed line might be related to the wave with slower velocity.

Center for Wave Phenomena
Department of Geophysics
Colorado School of Mines
1500 Illinois Street
Golden, Colorado 80401
nnakata@mines.edu
rsnieder@mines.edu
(N.N., R.S.)

National Institute for Rural Engineering
2-1-6 Kannondai, Tsukuba-shi
Ibaraki 305-8609 Japan
skuroda@affrc.go.jp
(S.K.)

Suncoh Consultants Co., Ltd.
1-8-9 Kameido, Koto-ku
Tokyo 136-8592 Japan
s.ito@suncoh.co.jp
aizawa@suncoh.co.jp
(S.I., T.A.)

Akebono Brake Industry Co., Ltd.
5-4-71 Higashi, Hanyu-shi
Saitama 348-8509 Japan
kunimi@akebono-brake.com
(T.K.)

Manuscript received 24 September 2012